

Filling the Pockets: The Spherical Nature of 3D Deflagration in Thermonuclear Supernovae

S. SHIBER,¹ P. HOEFLICH,¹ T. MERA,¹ E. FEREIDOUNI,¹ Z. LEVY,¹ D. MACI,² C. ASHALL,³ E. BARON,^{4,5}
 M. SHAHBADEH,⁶ K. MEDLER,³ W. B. HOOGENDAM,^{3,*} AND C. M. PFEFFER^{3,*}

¹Department of Physics, Florida State University, 77 Chieftan Way, Tallahassee, FL 32306, USA

²Centre for mathematical Plasma Astrophysics, Department of Mathematics, KU Leuven, Celestijnenlaan 200B, B-3001 Leuven, Belgium

³Institute for Astronomy, University of Hawai'i at Manoa, 2680 Woodlawn Dr., Hawai'i, HI 96822, USA

⁴Planetary Science Institute, 1700 East Fort Lowell Road, Suite 106, Tucson, AZ 85719-2395 USA

⁵Hamburger Sternwarte, Gojenbergsweg 112, 21029 Hamburg, Germany

⁶Space Telescope Science Institute, 3700 San Martin Drive, Baltimore, MD 21218-2410, USA

(Received February 13, 2026; Revised February 13, 2026; Accepted February 13, 2026)

Submitted to ApJ

ABSTRACT

We investigate thermonuclear explosions within the delayed detonation framework. While spherical delayed detonation models generally reproduce key observational features, a fundamental inconsistency emerges in three dimensions: 3D hydrodynamic simulations exhibit insufficient white dwarf expansion during the deflagration phase. We identify the early deflagration stage, when the burning is dominated by the laminar speed, as a critical phase and explore potential solutions using three-dimensional magnetohydrodynamic simulations performed with the FLASH code. In hydrodynamical simulations, the early deflagration phase produces large pockets of unburned C/O, leading to inefficient burning. Much of the released energy is deposited into buoyantly rising plumes rather than into the global pre-expansion of the white dwarf, which is required to produce the partially burned layers characteristic of SNe Ia. In contrast, when preexisting turbulent velocity fields and strong magnetic fields, on scales expected from the smoldering phase, are included, the effective burning approaches that in spherical models. Both turbulence and magnetic fields promote the entrainment of burned material into unburned pockets, addressing a long-standing problem in multi-dimensional deflagration models. The resulting streaks of burned material enable the conductive ignition of the surrounding unburned fuel. The dominant effect is not a change in the small-scale flame physics ($\sim 10^{-3}$ cm), but rather enhanced mixing between burned and unburned material. As expected, this mechanism is most efficient when the turbulent length scales are smaller than those of the unburned plumes.

Keywords: Type Ia supernovae, Magnetohydrodynamics, Magnetohydrodynamical simulations, Plasma astrophysics

1. INTRODUCTION

Type Ia supernovae (SNe Ia) are generally agreed to arise from thermonuclear explosions of carbon-oxygen (C/O) white dwarfs (WDs) (e.g., Hoyle & Fowler 1960, Whelan & Iben 1973, Piersanti et al. 2003, and also recent reviews by Liu et al. 2023, Ruiter & Seitenzahl 2025, and references therein). Despite much effort and investigation, the community has yet not come to a con-

sensus, neither regarding the progenitor system nor the main mechanism causing the explosion.

In fact, many recent observational and theoretical studies show an intrinsic diversity of SN Ia (Hoogendam et al. 2025a,b; Bose et al. 2025a,b; Dimitriadis et al. 2025; Paniagua et al. 2026). With tuning, most currently favored explosion scenarios can reproduce the overall light curves (LCs) and total flux spectra because nuclear physics governs the progenitor structure, abundances, and explosion energies, a fact described as “stellar amnesia”. To truly understand a given event is challenging because the WD can explode in different ways,

* National Science Foundation Graduate Research Fellow

leading to even more varied burning products, and because it can have evolved in very different progenitor systems, resulting in numerous possible interactions between the SN ejecta and components of the progenitor.

Three leading scenarios are *I) Explosion of a near- M_{Ch} WD*: The flame starts close to the high-density center, producing electron-capture (EC) elements. The resulting structures depend on preexisting turbulence (Höflich & Stein 2002), magnetic fields, and develop Rayleigh-Taylor (RT) instabilities. Subsequently, the flame transitions to a detonation (Khokhlov 1991, 1995; Niemeyer et al. 1996; Poludnenko et al. 2019; Brooker et al. 2021; Hristov et al. 2021), occurring off-center, leading to asymmetric line profiles and polarization signatures with high-density burning probed by stable EC elements. *II) Sub- M_{Ch} explosions*: The explosion is triggered by a surface He-detonation that triggers a second detonation in the C/O core of the WD (Woosley et al. 1980; Nomoto 1982a; Livne 1990; Woosley & Weaver 1994; Höflich & Khokhlov 1996; Kromer et al. 2010; Sim et al. 2010; Woosley & Kasen 2011; Shen 2015; Tanikawa 2018; Glasner et al. 2018; Shen et al. 2018; Townsley et al. 2019). Fundamental characteristics are low-density burning with little production of EC elements, with a significant amount only produced by super-solar metallicity WDs (Blondin et al. 2022), and a rather spherical distribution of iron-group elements in the core. *III) Hydrodynamical, violent, and secular mergers*: Detonations are triggered by collisions, possibly head-on in a triple system, or by compressional heating (Webbink 1984; Iben & Tutukov 1984; Benz et al. 1990; Rasio & Shapiro 1994; Höflich & Khokhlov 1996; Segretain et al. 1997; Yoon et al. 2007; Wang et al. 2009b,a; Lorén-Aguilar et al. 2009; Pakmor et al. 2011; Isern et al. 2011; Pakmor et al. 2012; Rosswog et al. 2009; Thompson 2011; Pejcha et al. 2013; Kushnir et al. 2013; Dong et al. 2015; García-Berro & Lorén-Aguilar 2017). The merger can also take place within the common envelope of an asymptotic giant branch (AGB) star and a WD (Hoeflich & Khokhlov 1996; Yoon et al. 2007; Kashi & Soker 2011; Hoeflich 2017). Simulations show ejecta with large-scale rotational symmetry in density that lead to continuum polarization (Patat et al. 2012), and spiral structures on small scales in iron-group elements with little EC elements. However, in violent and secular mergers of two WDs, with $M_{\text{WD}} \geq 0.7M_{\odot}$ each, high-density burning and EC elements are expected because it will form hydrostatic WD stabilized by rotation, shrinking by subsequent loss of angular momentum.

Recently, the ubiquity of EC elements has been well established (Galbany et al. 2019; Blondin et al. 2022; DerKacy et al. 2023, 2024; Ashall et al. 2024; Kumar

et al. 2025; Kwok et al. 2025), suggesting high density burning. This favors near- M_{Ch} scenarios or secular mergers. However, low continuum polarization values are observed in the early phase of many SNe, disfavoring the merger scenario. Spectropolarimetry confirmed an overall small deviation from sphericity, but also pointed towards a large-scale asymmetry in the abundance structure, suggesting that the transition from deflagration to detonation occurs off-center (Yang et al. 2020; Patra et al. 2022; Hoeflich et al. 2023; Cikota et al. 2026).

Though spherical delayed-detonation models (Khokhlov 1991) have been shown to agree with the lightcurve and the optical to mid-IR spectra (Hoeflich et al. 2017; DerKacy et al. 2023; Ashall et al. 2024; DerKacy et al. 2024), the ignition and propagation of the flame are inherently multi-dimensional. Turbulence, deflagration–detonation transitions, and incomplete burning introduce asphericities that influence nucleosynthesis yields and emergent spectra. In spherical geometry, the pre-expansion required is consistent with observations. However, three-dimensional (3D) simulations produce large-scale instabilities, and most of the energy goes into the rise of burned plumes (Khokhlov 1991; Gamezo et al. 2003; Röpke et al. 2003) rather than pre-expansion. The ratio between burned and unburned material remains small.

The key question to be addressed is the influence of preexisting turbulence, produced during the smoldering phase prior to the explosion, and the influence of magnetic fields on the early deflagration. To address these questions, we present the results of full 3D simulations which include both high turbulent fields and B fields. In Section 2, we focus on the magnetic properties present in WDs at the beginning of the deflagration phase. In Section 3, we describe our numerical methods. The results are discussed and conclusions are presented in Section 4 and 5.

2. MAGNETIC PROPERTIES

Typically, low magnetic fields are found in WDs (Liebert et al. 2003). However, observations of late-time LCs, line profiles, and spectra suggest the existence of high-magnetic fields in excess of $\approx 10^6 - 10^7$ G (e.g., Diamond et al. 2018; Hristov et al. 2021). A seed magnetic field can be amplified by a dynamo operating in the convective zone or by large-scale circulation in WDs (Parker 1979; Thomas et al. 1995; Brandenburg & Subramanian 2005; Desai et al. 2025).

In large-scale dynamos, a toroidal field is produced by winding up the poloidal component. The convective elements move upward and downward, perpendicular to the toroidal field, creating a new poloidal com-

ponent (Parker 1979). Alternatively, in small-scale dynamos, convection alone can produce a small-scale unstructured magnetic field (Brandenburg & Subramanian 2005; Beresnyak 2012; Tayler 1973; Acheson 1978; Hawley et al. 1996; Spruit 2002; Braithwaite 2009; Duez et al. 2010b,a). Within dynamo theory and ideal magnetohydrodynamics (MHD), the maximum size of the B field in WDs may approach saturation strength of $10^9 - 10^{11}$ G in WDs (Chandrasekhar 1956; Chandrasekhar & Prendergast 1956; Mestel 1956). Large-scale dynamos grow with a typical time scale of the Alfvén time, $t_A \approx R(4\pi\rho)^{1/2}B^{-1} \approx 300$ s (Parker 1979), while small-scale dynamos grow from small scale to large with a timescale of $\approx Lv^{-1} \approx 1$ s where L and v are the characteristic scale and velocity.

In short, the amplification of the magnetic field is driven by either of the following dynamo mechanisms: I) due to accretion over many years; II) due to turbulent burning prior to the runaway, i.e., during the smoldering phase (Höflich & Stein 2002); III) due to RT instabilities and magnetic entanglement during the deflagration phase (Hristov et al. 2018); or IV) due to instabilities induced by ^{56}Ni -decay over time-scales of several days after the explosion (see Fesen et al. 2018 for supporting evidence of caustic structure in SN1885).

3. NUMERICAL SETUP OF THE SIMULATIONS

We use the multi-physics code **FLASH** (Fryxell et al. 2000), version 4.8, to carry out 3D MHD simulations of centrally ignited deflagration front embedded within turbulent velocity and magnetic fields in a near- M_{Ch} WD. The WD structure originated from a $7 M_{\odot}$ zero-age-main-sequence star of solar metallicity that accretes hydrogen (and helium) from a companion. The accretion rate is adjusted to lead to a thermodynamic runaway at a central density of $\approx 10^9$ g cm $^{-3}$ (Hoeflich et al. 2017) similar to the scheme of (Sugimoto & Nomoto 1980; Nomoto 1982b). Following the accretion, the WD contracts to a radius of 2,000 km.

We map the WD structure to the 3D Cartesian cubical grid of **FLASH**. To accommodate turbulence of varying scale sizes, our simulations differ in resolution. The base resolution in all of our simulations consists of $[32 \times 32 \times 32]$ cells, which corresponds to **FLASH**'s three levels of refinement, while the maximal refinement level l_{max} spans from 7 to 10. The grid is logarithmically refined from the center out, while ensuring that the innermost region is refined to the maximal level. With a domain size of 5×10^3 km, this corresponds to a minimal cell size of $dx_{\text{min}} = 10$ km, 2.5 km, and 1.2 km for $l_{\text{max}} = 7, 9$, and 10, respectively.

Due to discretization errors, the WD begins to pulsate; therefore, we damp the velocity for 0.1 s, while simultaneously holding a spherical boundary at 1,500 km around the center. The gravity is computed according to **FLASH**'s Poisson multipole solver with a highest multipole order of 16 and isolated boundary conditions. A Helmholtz equation of state (EoS) for gas with degenerate electrons is used (Timmes & Swesty 2000). This EoS includes contributions to energy and pressure from degenerate electrons–positrons, thermal ions, radiation, and Coulomb corrections.

The deflagration is modeled according to the advection-diffusion-reaction (ADR) scheme (Khokhlov 1995) with a sharpened Kolmogorov Petrovski Piskunov (sKPP) reaction term (Vladimirova et al. 2006), where default values for ϵ_0 , ϵ_1 , f , and b were used (see Townsley et al. 2007). Since we focus on the early phase of the deflagration, where the front remains in regions with densities $> 10^7$ g cm $^{-3}$, we assume nuclear statistical equilibrium (NSE) burning, which is tracked by a scalar field ϕ (zero means unburnt C/O mixture, while one means full NSE burning to iron group elements of mostly ^{56}Ni). The burning front propagates at a constant laminar speed of 200 km s $^{-1}$, and the nuclear (specific) energy deposition rate is: $\dot{E}_{\text{nuc}} = (\phi/m_p) \times [\tilde{b}_{\text{Ni}} - (1 - X_{\text{C}})\tilde{b}_{\text{O}} - X_{\text{C}}\tilde{b}_{\text{C}}]$, where \tilde{b}_{Ni} , \tilde{b}_{O} , and \tilde{b}_{C} are the binding energies per nucleon of ^{56}Ni , ^{16}O , and ^{12}C , respectively. In the WD model, the core is depleted of carbon and $X_{\text{C}} = 0.278$ (up to a radius of $\lesssim 900$ km). Therefore, we assume this composition for the entire simulation evolution and set the energy deposition rate to $\dot{E}_{\text{nuc}} = 7.19 \times 10^{17}\phi$ erg g $^{-1}$. In addition, we do not change the composition according to the burning, which might have a small effect on the temperature. To prevent substantial motion from non-equilibrium perturbations, we keep the spherical boundary at 1,500 km stationary during the evolution.

For the initialization, a fully developed turbulent field has been constructed using the BxC toolkit. The BxC toolkit is designed to generate fully customizable synthetic turbulent 3D magnetic fields that include both turbulent structures and higher-order statistics (Durrive et al. 2022; Maci et al. 2024). A turbulence with v_{rms} up to 500 km/sec, resulting in a size of the turbulent eddies of up to ≈ 50 km, has been shown to form during the smoldering phase (see Fig. 8 of Höflich & Stein 2002). We adjust the turbulence properties to closely follow these physical conditions, i.e., we set the diffusion radius of the Kolmogorov spectrum to ≈ 50 km and the v_{rms} up to ≈ 200 km/sec.

Hristov et al. (2021) found that an initial large-scale dipole magnetic field has become turbulent during the

deflagration phase. Consequently, it can be expected that the morphology of the magnetic field would become turbulent even before the deflagration starts, and a turbulent magnetic field would develop during the smoldering phase before the runaway. Therefore, we assumed the same morphology of the initial B field as the turbulence. The magnetic field strength can be larger than the minimal values of $10^6 - 10^7$ G suggested by observations. The amplification depends on the dynamo time-scales prior to the runaway, and can grow up to the limit of equilibrium between the magnetic field and plasma (equi-partition field). Here, we consider fields up to 10^{12} G, a few percent of the equi-partition field.

To solve the MHD equations, we use **FLASH**'s unsplit staggered mesh solver, which ensures the divergence-free constraint of the magnetic fields by default. We assume ideal MHD, and use a hybrid type of Riemann solver, combining both the Roe solver for high accuracy and HLLD for stability.

In Figure 1, we show the initial turbulent conditions in the equatorial, xy , plane of our smallest-scale turbulence simulation, D40V170B12. On the left panels, we present the velocity magnitude, while the magnetic field magnitude is presented on the right. In the upper panels, a large scale view is shown with a representation of our adaptive grid, while in the lower panels, we zoom into the most refined, 300 km central regions. The ≈ 50 km eddies are clearly shown in the lower panels. For this simulation, $v_{\text{rms}} = 170$ km/s and $B_{\text{rms}} = 7 \times 10^{11}$ G. Outside of this most inner region, the turbulent pattern is duplicated. The properties of our simulations are summarized in Table 1.

4. RESULTS

We initiate the simulations by igniting the most central 100 km of the WD. We evolve the simulations until $t = 0.5$ s and follow the propagation of the deflagration to study the effect of preexisting turbulent magnetic and velocity fields on the efficiency of burning. We stopped at $t = 0.5$ s because in this study we focus only on the early evolution. By this time, the maximum distance that the deflagration front has reached in our simulations is $\lesssim 1000$ km. This is less than 2/3 of the static boundary at 1,500 km, and therefore the boundary has only a marginal effect on our results.

In Figure 2, we show the evolution of the deflagration in our simulations. In each panel, we plot the fraction of burned material, ϕ , in the equatorial plane. The deflagration front starts to propagate with the laminar speed by heat conduction (upper row). Subsequently, RT instabilities begin to develop, creating plumes of burned material (middle row) that rapidly move outward due to

buoyancy forces (lower row). These rising plumes can leave large pockets of unburnt material between them, which cannot be reached by the laminar front. The size of these pockets can be approximated as the largest distance between two adjacent rising plumes. For pure hydrodynamic simulation (D300V30B0; first column from left), we find a pocket size of ≈ 100 km.

However, turbulence drags the burned material into these pockets through passive flow. Moreover, a Lorentz force acts perpendicularly to the motion of the rising plumes, curving the deflagration front, and consequently filling the pockets more efficiently. The key factor is the size of the turbulence smallest-scale (i.e., the diffusion radius). This is most notable in comparing between simulations D80V170B12 and D40V170B12 (second and third columns). These simulations are identical in their turbulence strength and magnetic field strength (see their initial kinetic and magnetic energies in Table 1), and only differ in their turbulence's diffusion radius. The small-scale turbulence in D40V170B12 bends the deflagration front more efficiently, allowing the laminar speed to consume the unburned matter. The general result is a reduction in the distance between the burned material.

In Figure 3, we show temperature slices along the equatorial meridional planes at $t = 0.45$ s. Again, the deflagration within the small-scale turbulence (D40V170B12; middle panels) burns the pockets away more efficiently compared to deflagration with the same magnetic strength and velocity magnitude, but with twice the turbulence size (D80V170B12; left panels). In the small scale turbulence (middle panels), the burning within a radius is more complete and resembles a spherical deflagration both in the xy (upper row) and xz (lower row) planes.

In simulation D40V50B9 the deflagration evolves more slowly compared to D40V170B12, even though they have the same small-scale turbulence. The reason is that D40V50B9 has a weaker magnetic field (three magnitudes less) and lower turbulent velocities (a factor of 3.3 less). Although the pockets are still similar in size, the total burned matter at a certain time is larger when stronger turbulent fields are present.

To quantify the efficiency of burning, we measure the volume occupied by completely burned material in enclosed spheres around the center and divide it by the enclosed volume of the sphere. In Figure 4, we plot this ratio, which we refer to as the filling factor, as a function of time for our four simulations and for eight different spheres. The spheres are 100 km apart, ranging from 100 km (the initial radius of ignition) to 800 km (about

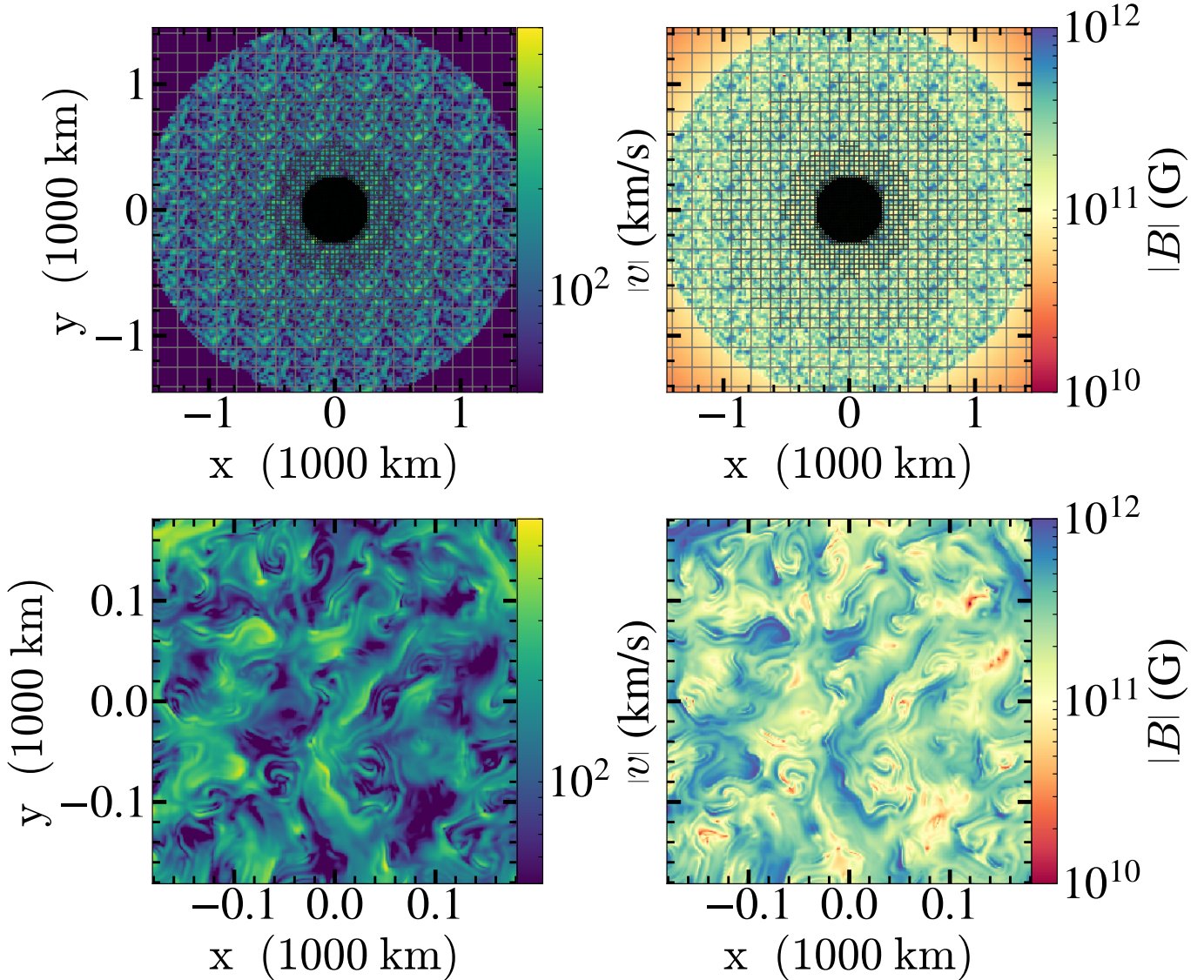


Figure 1. The initial turbulent velocity (left) and magnetic (right) fields in the highest resolution smallest-scale turbulence simulation D40V170B12, corresponding to smallest eddies size of roughly 40 km (Kolmagorov’s diffusion scale), a rms velocity of 170 km s^{-1} and a rms magnetic field of $7 \times 10^{11} \text{ G}$. The upper row presents the full grid while the lower row presents a zoom-in view of the central most refined region.

half of our boundary radius). We also plot the maximal distance of the deflagration front from the center.

In pure hydrodynamic simulations or in simulations with large-scale turbulent fields, the filling factor for most radii is smaller than $\approx 10\%$, and even in the central 200 km it reaches only 0.35. The burning is not complete and far away from spherical deflagration models in which the filling factor is exactly 1 inside the deflagration front.

Turbulent fields with eddies that are similar in size to the pockets or slightly larger result in a drag of the unburned material, effectively increasing the filling factors. Small-scale turbulence fields with eddy sizes that are smaller than the pockets result in efficient mixing

of the plumes with the fuel, burning the pockets away. This leads to efficiencies that exceed 75% in the inner 400 km of the WD. The burning in this simulation is much closer to a spherical model. Note that later on high B fields also cause a faster decay of large-scale eddies and therefore suppress large-scale mixing of burning products in the radial direction (Hristov et al. 2018).

Figure 4 panel (e) shows the filling factor as a function of the radius from the center at $t = 0.45 \text{ s}$, demonstrating the substantially more efficient burning in small-scale turbulence with strong fields. The maximal distance of the deflagration front in that instance of time is also plotted for each simulation as a vertical line. In

Simulation	r_D (km)	v_{rms} (km/s)	B_{rms} (G)	l_{max}	E_{kin}^i (erg)	E_{mag}^i (erg)	$r_{\text{max}}^{t=0.5}$ (km)	$f_{300}^{t=0.5}$	$f_{500}^{t=0.5}$	$E_{\text{nuc}}^{t=0.5}$ (erg)	$E_{\text{kin}}^{t=0.5}$ (erg)
D300V30B0	300	30	0	7	3.2×10^{46}	0	400	0.11	0.02	1.7×10^{49}	3.2×10^{47}
D80V170B12	80	170	7×10^{11}	9	2.4×10^{47}	5.8×10^{46}	830	0.50	0.24	6.8×10^{49}	3.6×10^{48}
D40V170B12	40	170	7×10^{11}	10	2.4×10^{47}	5.7×10^{46}	990	0.85	0.59	1.5×10^{50}	8.5×10^{49}
D40V50B9	40	50	7×10^9	10	2.3×10^{46}	5.8×10^{40}	750	0.71	0.30	6.5×10^{49}	2.4×10^{48}

Table 1. Properties of our simulations. The binding energy of the WD (sum of gravitational potential and internal energy) is $E_{\text{bind}} = 4.8 \times 10^{50}$ erg. Each simulation is given a name based on their smallest scale diffusion radius (r_D) of the turbulence, DXXX, follows by the turbulence velocity rms (v_{rms}), VXXX, and \log_{10} of the magnetic field rms (B_{rms}), BX (note tough that B0 is a pure hydrodynamic simulation). The maximal level of refinement l_{max} , the initial kinetic and magnetic energy are additionally shown (columns 3-5). The rightmost five columns show deflagration status at $t = 0.5$ s, when we stopped our simulations. r_{max} is the maximal distance of the deflagration front from the center, f_{300} , and f_{500} are the fractions of burnt mass inside a sphere of 300, and 500, km, respectively. E_{nuc} and E_{kin} are the total deposited nuclear energy and kinetic energy, respectively.

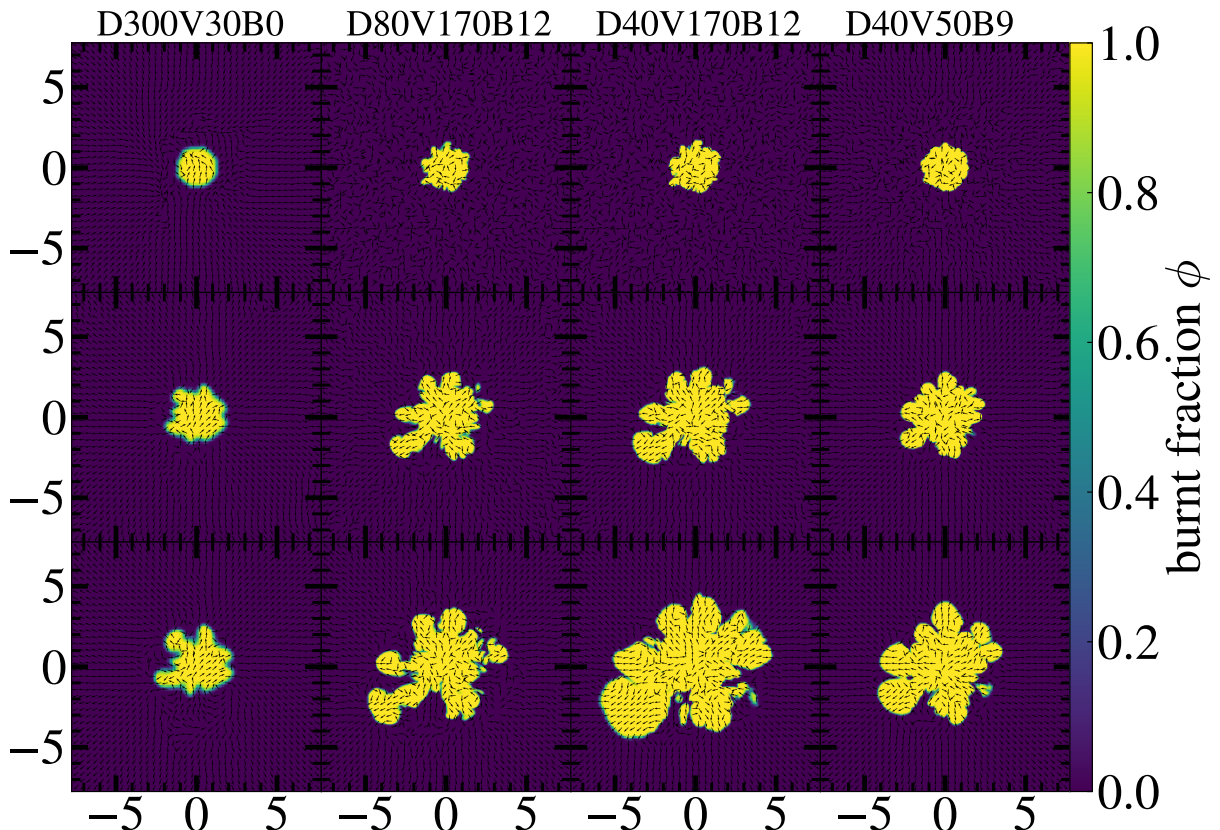


Figure 2. Fraction of burnt material at three times, $t = 0.15, 0.35, 0.45$ s (top, middle, bottom panels, respectively), at the equatorial plane comparing our simulations. The axes are in units of 100 km. From left to right, the simulations shown are: D300V30B0, D80V170B12, D40V170B12, D40V50B9 as denoted at the top of each column. Velocity vectors are plotted as black arrows.

the small-scale strong turbulence simulation, the deflagration has consistently higher filling factors at all radii.

Lastly, Figure 4 panel (f) presents the kinetic energy in our simulations as a function of time. The simulations with slower turbulence evolve more slowly, and the deposition of energy is significantly less (see column $E_{\text{nuc}}^{t=0.5}$ on the right side of Table 1). Between simulations of fast turbulence, the small-scale turbulence resulted in a

more efficient and faster deposition of nuclear energy. As a result, a more significant pre-expansion of the star would take place when the deflagration propagates outward and potentially detonates. Moreover, in this simulation, D40V170B12, the kinetic energy after $t = 0.5$ s is about half of the deposited nuclear energy (see again the two right columns in Table 1). This fraction is substantially larger than the other simulations. During the early

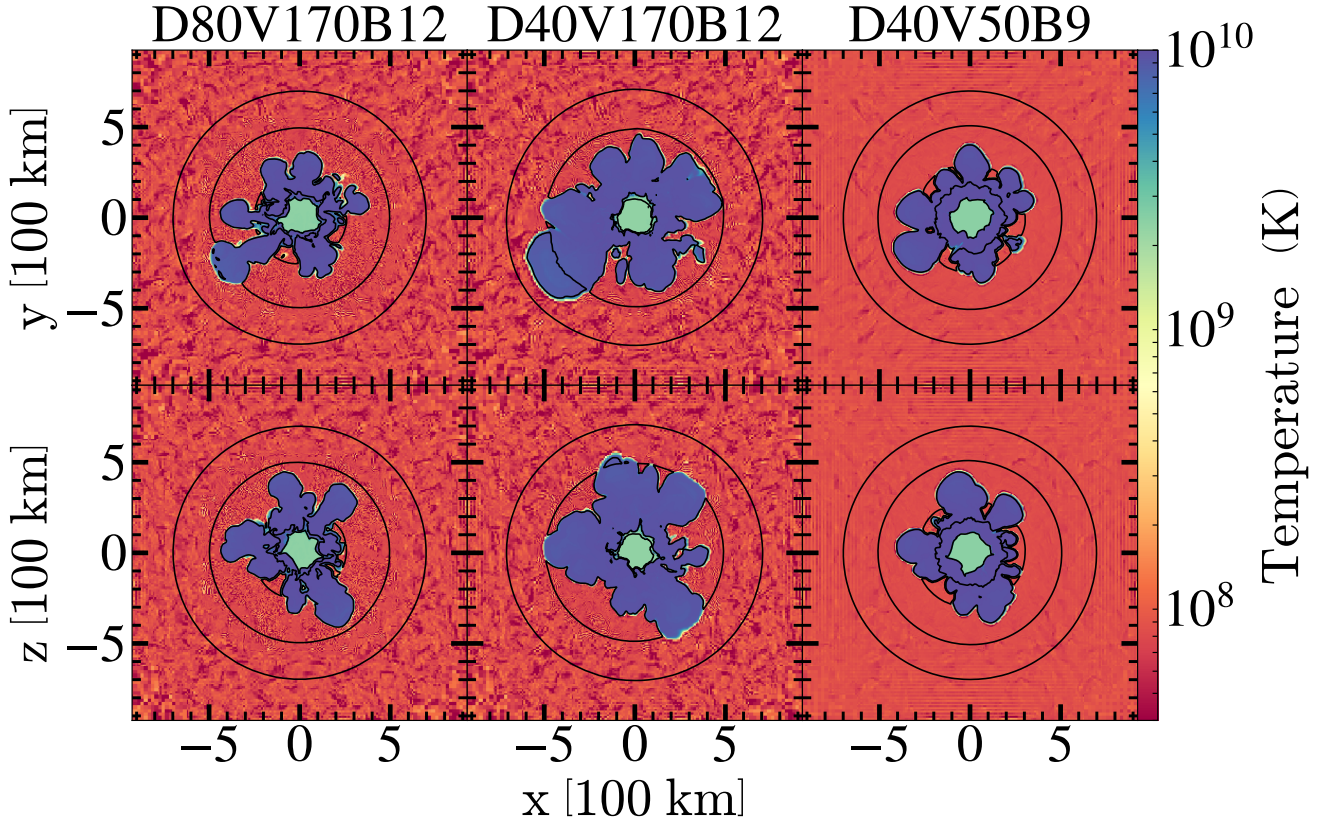


Figure 3. Temperature slices at $t = 0.45$ s of the equatorial (top row) and meridional (bottom row) planes, comparing 3 selected simulations with different magnetic field strengths and turbulent conditions. From left to right, the simulations shown are: larger-scale, strong turbulence simulation D80V170B12, smaller-scale, strong turbulence simulation D40V170B12, and smaller-scale, weak turbulence simulation D40V50B9 (denoted at the top of each column).

phase, the turbulence injects hot-burned material into the unburned pockets, reducing the distance between burned and unburned material. This allows the pockets to be burned with the laminar burning speed. As a result, the deposited nuclear energy goes into the expansion of the WD rather than producing rising plumes in a mostly static WD.

5. CONCLUSIONS

We presented a series of simulations demonstrating that preexisting small-scale turbulent fields and turbulent B fields result in a qualitative change in the explosion of near- M_{Ch} mass WDs. We examined various turbulence conditions with different diffusion radii ($r_{\text{D}} = 40, 80, 300$ km), turbulent velocities ($v_{\text{rms}} = 30, 50, 170$ km/s) and turbulent magnetic field strengths ($B_{\text{rms}} = 0, 10^9, 10^{12}$ G) (see Table 1 and Figure 1 for a snapshot of a simulation with small-scale strong turbulence fields D40V170B12 at $t = 0$ s), finding that turbulence and magnetic fields drag the burned material into unburned pockets. The turbulent fields entrain the deflagration front, effectively reducing the distance between the burned and unburned components,

such that the laminar front is able to burn the fuel (Figures 2-4). This qualitative change serves as a first step towards a solution to the long-standing problem of insufficient expansion of the WD due to incomplete burning during the deflagration phase, as found in previous multidimensional studies (see Section 1).

Overall, based on our results, we conclude the following:

- High magnetic and turbulent fields have a significant impact on the early development of the flame. We note that preexisting turbulence must be expected from the pre-explosive burning (see Section 1; and Höflich & Stein 2002; Zingale et al. 2011). Evidence for high magnetic fields is related to late-time LCs and spectra (see Section 2; and Hristov et al. 2021).
- In pure hydrodynamic simulations or simulations with large-scale turbulent fields, such as in Gamezo et al. (2003) and simulation D300V30B0 of this study (left column of Figure 2), the early burning phase can be characterized by large pockets of unburned material. The burned material

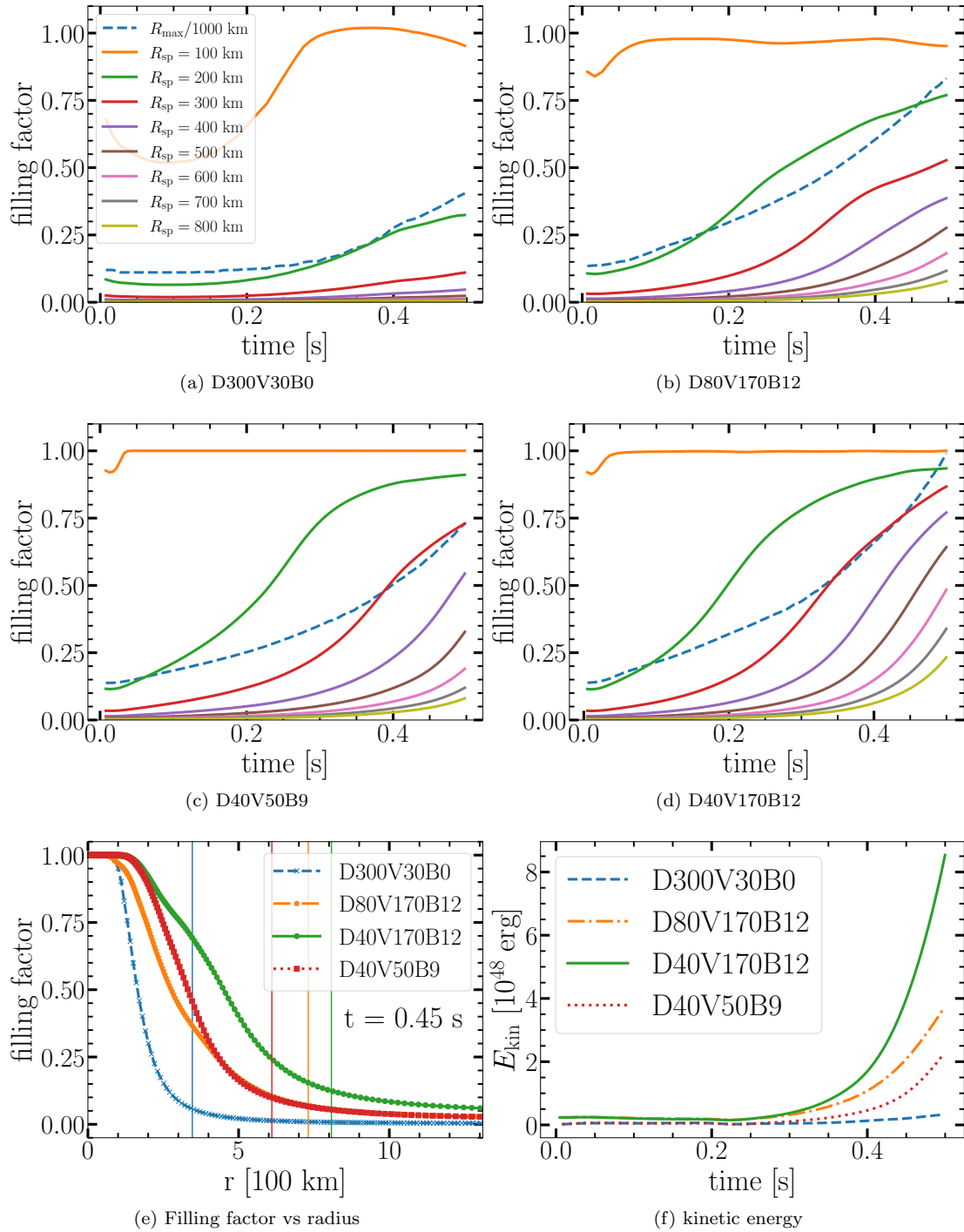


Figure 4. Panels (a),(b), (c), and (d): filling factors as a function of time of our simulations. Shown is the enclosed burnt volume fraction of eight spheres around the center with radii from 100 km to 800 km in jumps of 100 km (orange to gold). Overplotted is the deflagration front distance from the center (in blue). Panel (e): filling factor as a function of radius of our simulations at $t = 0.45$ s. The vertical lines denote the distance of the deflagration front from the center. Panel (f): kinetic energy as a function of time.

consists at most of only $\approx 10\%$ of the volume. As a consequence, the burning energy mainly drives the rise of the burned plumes rather than the expansion of the WD (panel (a) of Figure 4).

- Turbulent velocity fields with eddies that are comparable in size to the pockets or slightly larger result in a drag of the unburned material (passive flow), effectively increasing the burning efficiency, but only to a level insufficient for a considerable expansion of the WD. (left panels of Figure 3 and Figure 4 panel (b)).
- Small-scale turbulence fields with eddy sizes that are smaller than the pockets result in an efficient mixing of the fuel into the plumes, burning the pockets away. This leads to efficiencies that exceed 75% in the inner 400 km of the WD, and a continuous increase of V_{eff} . As a sequence, these 3D simulations approach to the evolution of spherical simulations resulting in a very effective expansion of the WD (Figure 4 panel (f)).

We must stress that although our high resolution simulation D40V179B12 yielded the most efficient burning, resolution alone cannot cause this qualitative difference. This has been shown (Poludnenko, private communication) through simulations with increasing resolution reaching a finer resolution than our simulations. It is also supported by simulation D40V50B9, which has the same resolution as D40V170B12, but weaker fields, and resulted in less pre-expansion. The crucial ingredient is the presence of turbulent fields, in particular, turbulence with sufficiently small eddies.

Finally, we want to emphasize the limitations of the current study. Here, we only considered central ignition. However, in a corresponding ongoing study, we investigate the role of preexisting fields on deflagration that starts off-center. In addition, in the present study we focus on the early deflagration phase up to 0.5 s. In a future study, we will simulate the entire deflagration phase. This will require the removal of our boundary condition at 1,500 km, and the inclusion of quasi-NSE and carbon burning. Varying the deflagration-to-detonation transition will allow us to qualitatively compare the models to a wide variety of SN observations,

including a direct comparison with the production of EC elements (see Section 1).

Although we showed that strong small-scale turbulent fields are likely essential for the overall evolution of the explosion and pave the way for the future, more detailed MHD studies of the initial conditions are needed. For example, our initial WD has a central density of $\approx 10^9 \text{ g cm}^{-3}$, a value typically found in observations (Section 1). In future studies, we will focus on WDs with higher central densities. Such high densities are expected to produce more EC elements, and therefore it would be specifically interesting to investigate the effects of turbulence fields on the production of EC elements in these cases.

ACKNOWLEDGEMENTS

Sa.S. and P.H., acknowledge the support by the National Science Foundation NSF awards AST-1715133 and AST-230639 for enabling the development of the methods and computational codes. P.H. acknowledge support from NASA grants JWST-GO-02114, JWST-GO-02122, JWST-GO-04522, JWST-GO-04217, JWST-GO-04436, JWST-GO-03726, JWST-GO-05057, JWST-GO-05290, JWST-GO-06023, JWST-GO-06677, JWST-GO-06213, JWST-GO-06583, JWST-GO-09231. C.A., K.M., W.B.H. and C.P. acknowledge support from NASA grants JWST-GO-02114, JWST-GO-02122, JWST-GO-03726, JWST-GO-04217, JWST-GO-04436, JWST-GO-04522, JWST-GO-05057, JWST-GO-05290, JWST-GO-06023, JWST-GO-06213, JWST-GO-06583, and JWST-GO-06677. Support for these programs was provided by NASA through a grant from the Space Telescope Science Institute, which is operated by the Association of Universities for Research in Astronomy, Inc., under NASA contract NAS5-03127. W.B.H. acknowledges support from the National Science Foundation Graduate Research Fellowship Program under Grant No. 2236415. This work also required using and integrating a Python package for astronomy, *yt* (<https://yt-project.org>, Turk et al. 2011).

Software: FLASH (Fryxell et al. 2000; Dubey et al. 2009, 2013, 2014, <https://flash.rochester.edu>), *yt* (Turk et al. 2011, <https://yt-project.org>), *BxC toolkit* (Durrive et al. 2022; Maci et al. 2024, <https://bxc.academy/>)

REFERENCES

Acheson, D. J. 1978, Royal Society of London Philosophical Transactions Series A, 289, 459

Ashall, C., Hoeflich, P., Baron, E., et al. 2024, ApJ, 975, 203, doi: [10.3847/1538-4357/ad6608](https://doi.org/10.3847/1538-4357/ad6608)

Benz, W., Cameron, A. G. W., Press, W. H., & Bowers, R. L. 1990, *ApJ*, 348, 647

Beresnyak, A. 2012, *Physical Review Letters*, 108, 035002. <https://arxiv.org/abs/1109.4644>

Blondin, S., Bravo, E., Timmes, F. X., Dessart, L., & Hillier, D. J. 2022, *A&A*, 660, A96, doi: [10.1051/0004-6361/202142323](https://doi.org/10.1051/0004-6361/202142323)

Bose, S., Stritzinger, M. D., Ashall, C., et al. 2025a, *A&A*, 699, A169, doi: [10.1051/0004-6361/202553687](https://doi.org/10.1051/0004-6361/202553687)

Bose, S., Stritzinger, M. D., Malmgaard, A., et al. 2025b, arXiv e-prints, arXiv:2511.07529, doi: [10.48550/arXiv.2511.07529](https://doi.org/10.48550/arXiv.2511.07529)

Braithwaite, J. 2009, *MNRAS*, 397, 763. <https://arxiv.org/abs/0810.1049>

Brandenburg, A., & Subramanian, K. 2005, *PhR*, 417, 1, doi: [10.1016/j.physrep.2005.06.005](https://doi.org/10.1016/j.physrep.2005.06.005)

Brooker, E., Plewa, T., & Fenn, D. 2021, *MNRAS*, 501, L23, doi: [10.1093/mnrasl/slaa141](https://doi.org/10.1093/mnrasl/slaa141)

Chandrasekhar, S. 1956, *Proceedings of the National Academy of Science*, 42, 273

Chandrasekhar, S., & Prendergast, K. H. 1956, *Proceedings of the National Academy of Science*, 42, 5

Cikota, A., Hoeflich, P., Baade, D., et al. 2026, *ApJL*, 996, L10, doi: [10.3847/2041-8213/ae27c8](https://doi.org/10.3847/2041-8213/ae27c8)

DerKacy, J. M., Ashall, C., Hoeflich, P., et al. 2023, *ApJL*, 945, L2, doi: [10.3847/2041-8213/acb8a8](https://doi.org/10.3847/2041-8213/acb8a8)

—. 2024, *ApJ*, 961, 187, doi: [10.3847/1538-4357/ad0b7b](https://doi.org/10.3847/1538-4357/ad0b7b)

Desai, D. D., Haggerty, C. C., Shappee, B. J., et al. 2025, *MNRAS*, 541, 2197, doi: [10.1093/mnras/staf1117](https://doi.org/10.1093/mnras/staf1117)

Diamond, T. R., Hoeflich, P., Hsiao, E. Y., et al. 2018, *ApJ*, 861, 119, doi: [10.3847/1538-4357/aac434](https://doi.org/10.3847/1538-4357/aac434)

Dimitriadis, G., Burgaz, U., Deckers, M., et al. 2025, *A&A*, 694, A10, doi: [10.1051/0004-6361/202451852](https://doi.org/10.1051/0004-6361/202451852)

Dong, S., Katz, B., Kushnir, D., & Prieto, J. L. 2015, *MNRAS*, 454, L61, doi: [10.1093/mnrasl/slv129](https://doi.org/10.1093/mnrasl/slv129)

Dubey, A., Antypas, K., Ganapathy, M. K., et al. 2009, *Parallel Computing*, 35, 512, doi: <https://doi.org/10.1016/j.parco.2009.08.001>

Dubey, A., Calder, A. C., Daley, C., et al. 2013, *The International Journal of High Performance Computing Applications*, 27, 360, doi: [10.1177/1094342012464404](https://doi.org/10.1177/1094342012464404)

Dubey, A., Antypas, K., Calder, A. C., et al. 2014, *Int. J. High Perform. Comput. Appl.*, 28, 225–237, doi: [10.1177/1094342013505656](https://doi.org/10.1177/1094342013505656)

Duez, M. D., Foucart, F., Kidder, L. E., Ott, C. D., & Teukolsky, S. A. 2010a, *Classical and Quantum Gravity*, 27, 114106. <https://arxiv.org/abs/0912.3528>

Duez, V., Braithwaite, J., & Mathis, S. 2010b, *ApJL*, 724, L34. <https://arxiv.org/abs/1009.5384>

Durriwe, J.-B., Changmai, M., Keppens, R., et al. 2022, *PhRvE*, 106, 025307, doi: [10.1103/PhysRevE.106.025307](https://doi.org/10.1103/PhysRevE.106.025307)

Fesen, R. A., Weil, K. E., Cisneros, I. A., Blair, W. P., & Raymond, J. C. 2018, *MNRAS*, 481, 1786, doi: [10.1093/mnras/sty2370](https://doi.org/10.1093/mnras/sty2370)

Fryxell, B., Olson, K., Ricker, P., et al. 2000, *ApJS*, 131, 273, doi: [10.1086/317361](https://doi.org/10.1086/317361)

Galbany, L., Ashall, C., Höflich, P., et al. 2019, *A&A*, 630, A76, doi: [10.1051/0004-6361/201935537](https://doi.org/10.1051/0004-6361/201935537)

Gamezo, V. N., Khokhlov, A. M., Oran, E. S., Chtchelkanova, A. Y., & Rosenberg, R. O. 2003, *Science*, 299, 77, doi: [10.1126/science.299.5603.77](https://doi.org/10.1126/science.299.5603.77)

García-Berro, E., & Lorén-Aguilar, P. 2017, in *Handbook of Supernovae*, ed. A. W. Alsabti & P. Murdin (Springer), 1237, doi: [10.1007/978-3-319-21846-5_60](https://doi.org/10.1007/978-3-319-21846-5_60)

Glasner, S. A., Livne, E., Steinberg, E., Yalinewich, A., & Truran, J. W. 2018, *MNRAS*, 476, 2238, doi: [10.1093/mnras/sty421](https://doi.org/10.1093/mnras/sty421)

Hawley, J. F., Gammie, C. F., & Balbus, S. A. 1996, *ApJ*, 464, 690

Hoeflich, P. 2017, in *Handbook of Supernovae*, ed. A. W. Alsabti & P. Murdin (Berlin: Springer), 1151, doi: [10.1007/978-3-319-21846-5_56](https://doi.org/10.1007/978-3-319-21846-5_56)

Hoeflich, P., & Khokhlov, A. 1996, *ApJ*, 457, 500, doi: [10.1086/176748](https://doi.org/10.1086/176748)

Hoeflich, P., Hsiao, E. Y., Ashall, C., et al. 2017, *ApJ*, 846, 58, doi: [10.3847/1538-4357/aa84b2](https://doi.org/10.3847/1538-4357/aa84b2)

Hoeflich, P., Yang, Y., Baade, D., et al. 2023, *MNRAS*, 520, 560, doi: [10.1093/mnras/stad172](https://doi.org/10.1093/mnras/stad172)

Höflich, P., & Khokhlov, A. 1996, *ApJ*, 457, 500

Höflich, P., & Stein, J. 2002, *ApJ*, 568, 779, doi: [10.1086/338981](https://doi.org/10.1086/338981)

Hoogendam, W. B., Ashall, C., Jones, D. O., et al. 2025a, *ApJ*, 988, 209, doi: [10.3847/1538-4357/ade787](https://doi.org/10.3847/1538-4357/ade787)

Hoogendam, W. B., Jones, D. O., Ashall, C., et al. 2025b, *The Open Journal of Astrophysics*, 8, 120, doi: [10.33232/001c.143462](https://doi.org/10.33232/001c.143462)

Hoyle, F., & Fowler, W. A. 1960, *ApJ*, 132, 565

Hristov, B., Collins, D. C., Hoeflich, P., Weatherford, C. A., & Diamond, T. R. 2018, *ApJ*, 858, 13, doi: [10.3847/1538-4357/aab7f2](https://doi.org/10.3847/1538-4357/aab7f2)

Hristov, B., Hoeflich, P., & Collins, D. C. 2021, *ApJ*, 923, 210, doi: [10.3847/1538-4357/ac0ef8](https://doi.org/10.3847/1538-4357/ac0ef8)

Iben, I., J., & Tutukov, A. V. 1984, *ApJS*, 54, 335, doi: [10.1086/190932](https://doi.org/10.1086/190932)

Isern, J., Hernanz, M., & José, J. 2011, in *Lecture Notes in Physics*, Berlin Springer Verlag, Vol. 812, *Lecture Notes in Physics*, Berlin Springer Verlag, ed. R. Diehl, D. H. Hartmann, & N. Prantzos, 233–308

Kashi, A., & Soker, N. 2011, MNRAS, 417, 1466, doi: [10.1111/j.1365-2966.2011.19361.x](https://doi.org/10.1111/j.1365-2966.2011.19361.x)

Khokhlov, A. M. 1991, A&A, 245, 114

—. 1995, ApJ, 449, 695

Kromer, M., Sim, S. A., Fink, M., et al. 2010, ApJ, 719, 1067, doi: [10.1088/0004-637X/719/2/1067](https://doi.org/10.1088/0004-637X/719/2/1067)

Kumar, S., Hsiao, E. Y., Ashall, C., et al. 2025, arXiv e-prints, arXiv:2504.17134, doi: [10.48550/arXiv.2504.17134](https://doi.org/10.48550/arXiv.2504.17134)

Kushnir, D., Katz, B., Dong, S., Livne, E., & Fernández, R. 2013, ApJL, 778, L37, doi: [10.1088/2041-8205/778/2/L37](https://doi.org/10.1088/2041-8205/778/2/L37)

Kwok, L. A., Liu, C., Jha, S. W., et al. 2025, arXiv e-prints, arXiv:2510.09760, doi: [10.48550/arXiv.2510.09760](https://doi.org/10.48550/arXiv.2510.09760)

Liebert, J., Bergeron, P., & Holberg, J. 2003, aj, 125, 348

Liu, Z.-W., Röpke, F. K., & Han, Z. 2023, Research in Astronomy and Astrophysics, 23, 082001, doi: [10.1088/1674-4527/acd89e](https://doi.org/10.1088/1674-4527/acd89e)

Livne, E. 1990, ApJL, 354, L53, doi: [10.1086/185721](https://doi.org/10.1086/185721)

Lorén-Aguilar, P., Isern, J., & García-Berro, E. 2009, A&A, 500, 1193

Maci, D., Keppens, R., & Bacchini, F. 2024, ApJS, 273, 11, doi: [10.3847/1538-4365/ad4bdf](https://doi.org/10.3847/1538-4365/ad4bdf)

Mestel, L. 1956, MNRAS, 116, 324

Niemeyer, J. C., Hillebrandt, W., & Woosley, S. E. 1996, ApJ, 471, 903, doi: [10.1086/178017](https://doi.org/10.1086/178017)

Nomoto, K. 1982a, ApJ, 257, 780, doi: [10.1086/160031](https://doi.org/10.1086/160031)

—. 1982b, ApJ, 253, 798, doi: [10.1086/159682](https://doi.org/10.1086/159682)

Pakmor, R., Edelmann, P., Röpke, F. K., & Hillebrandt, W. 2012, MNRAS, 424, 2222, doi: [10.1111/j.1365-2966.2012.21383.x](https://doi.org/10.1111/j.1365-2966.2012.21383.x)

Pakmor, R., Hachinger, S., Röpke, F. K., & Hillebrandt, W. 2011, A&A, 528, A117. <https://arxiv.org/abs/1102.1354>

Paniagua, I. A. A., Hoogendam, W. B., Jones, D. O., et al. 2026, ApJ, 997, 261, doi: [10.3847/1538-4357/ae279b](https://doi.org/10.3847/1538-4357/ae279b)

Parker, E. N. 1979, Cosmical magnetic fields: Their origin and their activity (New York: Oxford University Press)

Patat, F., Höflich, P., Baade, D., et al. 2012, A&A, 545, A7, doi: [10.1051/0004-6361/201219146](https://doi.org/10.1051/0004-6361/201219146)

Patra, K. C., Yang, Y., Brink, T. G., et al. 2022, MNRAS, 509, 4058, doi: [10.1093/mnras/stab3136](https://doi.org/10.1093/mnras/stab3136)

Pejcha, O., Antognini, J. M., Shappee, B. J., & Thompson, T. A. 2013, MNRAS, 435, 943, doi: [10.1093/mnras/stt1281](https://doi.org/10.1093/mnras/stt1281)

Piersanti, L., Gagliardi, S., Iben, Jr., I., & Tornambé, A. 2003, ApJ, 598, 1229

Poludnenko, A. Y., Chambers, J., Ahmed, K., Gamezo, V. N., & Taylor, B. D. 2019, Science, 366, aau7365, doi: [10.1126/science.aau7365](https://doi.org/10.1126/science.aau7365)

Rasio, F. A., & Shapiro, S. L. 1994, ApJ, 432, 242

Röpke, F. K., Niemeyer, J. C., & Hillebrandt, W. 2003, ApJ, 588, 952, doi: [10.1086/374216](https://doi.org/10.1086/374216)

Rosswog, S., Kasen, D., Guillot, J., & Ramirez-Ruiz, E. 2009, ApJL, 705, L128, doi: [10.1088/0004-637X/705/2/L128](https://doi.org/10.1088/0004-637X/705/2/L128)

Ruiter, A. J., & Seitzenzahl, I. R. 2025, A&A Rv, 33, 1, doi: [10.1007/s00159-024-00158-9](https://doi.org/10.1007/s00159-024-00158-9)

Segretain, L., Chabrier, G., & Mochkovitch, R. 1997, ApJ, 481, 355

Shen, K. J. 2015, ApJL, 805, L6, doi: [10.1088/2041-8205/805/1/L6](https://doi.org/10.1088/2041-8205/805/1/L6)

Shen, K. J., Kasen, D., Miles, B. J., & Townsley, D. M. 2018, ApJ, 854, 52, doi: [10.3847/1538-4357/aaa8de](https://doi.org/10.3847/1538-4357/aaa8de)

Sim, S. A., Röpke, F. K., Hillebrandt, W., et al. 2010, ApJL, 714, L52, doi: [10.1088/2041-8205/714/1/L52](https://doi.org/10.1088/2041-8205/714/1/L52)

Spruit, H. C. 2002, A&A, 381, 923

Sugimoto, D., & Nomoto, K. 1980, SSRv, 25, 155, doi: [10.1007/BF00212318](https://doi.org/10.1007/BF00212318)

Tanikawa, A. 2018, ApJ, 858, 26, doi: [10.3847/1538-4357/aaba79](https://doi.org/10.3847/1538-4357/aaba79)

Taylor, R. J. 1973, MNRAS, 161, 365

Thomas, J. H., Markiel, J. A., & van Horn, H. M. 1995, ApJ, 453, 403, doi: [10.1086/176400](https://doi.org/10.1086/176400)

Thompson, T. A. 2011, ApJ, 741, 82, doi: [10.1088/0004-637X/741/2/82](https://doi.org/10.1088/0004-637X/741/2/82)

Timmes, F. X., & Swesty, F. D. 2000, ApJS, 126, 501, doi: [10.1086/313304](https://doi.org/10.1086/313304)

Townsley, D. M., Calder, A. C., Asida, S. M., et al. 2007, ApJ, 668, 1118, doi: [10.1086/521013](https://doi.org/10.1086/521013)

Townsley, D. M., Miles, B. J., Shen, K. J., & Kasen, D. 2019, ApJL, 878, L38, doi: [10.3847/2041-8213/ab27cd](https://doi.org/10.3847/2041-8213/ab27cd)

Turk, M. J., Smith, B. D., Oishi, J. S., et al. 2011, ApJ, 192, 9, doi: [10.1088/0067-0049/192/1/9](https://doi.org/10.1088/0067-0049/192/1/9)

Vladimirova, N., Weirs, V. G., & Ryzhik, L. 2006, Combustion Theory and Modelling, 10, 727, doi: [10.1080/13647830500464146](https://doi.org/10.1080/13647830500464146)

Wang, B., Chen, X., Meng, X., & Han, Z. 2009a, ApJ, 701, 1540. <https://arxiv.org/abs/0906.4148>

Wang, B., Meng, X., Chen, X., & Han, Z. 2009b, MNRAS, 395, 847. <https://arxiv.org/abs/0901.3496>

Webbink, R. F. 1984, ApJ, 277, 355, doi: [10.1086/161701](https://doi.org/10.1086/161701)

Whelan, J., & Iben, I. J. 1973, ApJ, 186, 1007

Woosley, S. E., & Kasen, D. 2011, ApJ, 734, 38, doi: [10.1088/0004-637X/734/1/38](https://doi.org/10.1088/0004-637X/734/1/38)

Woosley, S. E., & Weaver, T. A. 1994, ApJ, 423, 371, doi: [10.1086/173813](https://doi.org/10.1086/173813)

Woosley, S. E., Weaver, T. A., & Taam, R. E. 1980, in Texas Workshop on Type I Supernovae, ed. J. C. Wheeler, 96–112

Yang, Y., Hoeflich, P., Baade, D., et al. 2020, ApJ, 902, 46,
doi: [10.3847/1538-4357/aba759](https://doi.org/10.3847/1538-4357/aba759)

Yoon, S.-C., Podsiadlowski, P., & Rosswog, S. 2007,
MNRAS, 380, 933. <https://arxiv.org/abs/0704.0297>
Zingale, M., Nonaka, A., Almgren, A. S., et al. 2011, ApJ,
740, 8